A Dual-Polarized Antenna Array With Enhanced Interport Isolation for Far-Field Wireless Data and Power Transfer

Zhang, Yiming; Li, Jia-Lin

Published in:
IEEE Transactions on Vehicular Technology

DOI (link to publication from Publisher):
10.1109/TVT.2018.2865415

Publication date:
2018

A Dual-Polarized Antenna Array With Enhanced Interport Isolation for Far-Field Wireless Data and Power Transfer

Yi-Ming Zhang, *Student Member, IEEE*, and Jia-Lin Li

***Abstract*—An in-band full-duplex scheme is proposed for simultaneous power transfer and data delivery in far-field wireless sensor systems. To realize two independent links for power and data delivery, a high isolation level between the local transmitter and receiver of the in-band full-duplex system is critical. An RF front-end architecture, here standing for a dual-polarized antenna array with its feeding network, is presented and detailed in this paper. By using the proposed architecture, self-interference can be well canceled within a wide frequency band, leading to a high inter-port isolation level. To demonstrate the performance of such a front-end structure, an on-board prototype has been developed and examined experimentally. Measured results show that the impedance bandwidth of the developed antenna is from 4.5 to 5.8 GHz. The achieved inter-port isolation is higher than 65 dB from 4.4 to over 6.0 GHz, and over 71 dB from 5.36 to 5.82 GHz, indicating a very high self-interference suppression level. Furthermore, RF power and video transferring experiments are carried out, and good consistency with calculated results is observed.**

***Index Terms*—Wireless powering, data delivery, in-band full-duplex, self-interference suppression.**

I. Introduction

RECENTLY, studies on far-field wireless sensor systems for vehicular applications have attracted increasing attentions, for instance, vehicular monitoring [1], [2], vehicular traffic and carbon dioxide pollution monitoring [3], [4]. Since the typically battery-based sensor has a limited lifetime and is not easy to be recharged in some far-field applications, wireless power transfer (WPT) technologies for wireless sensor systems are becoming hot-topics [5]–[20]. For a well-organized wireless sensor system with wireless powering, it has two parts [16]–[18]: the primary side and the pickup side. The primary side transmits power to the pickup side and receives data from the pickup side simultaneously. Similarly, the pickup side receives power and at the same time, delivers data to the primary side. In this process, the leakage between local power link and data link would influence the reliability and stabilization of data receiving at the primary side, and reduce the efficiency of the power receiving at the pickup side. Consequently, providing independent links to deliver power and data for both sides is a basic issue and of great significance [12], [15]–[20].

Using the frequency-division duplex (FDD) technique is one of the common methods for separating power and data links [13], [18], [19]. Low-power wireless sensors based on FDD technique were discussed in [13], where a frequency of 2.45 GHz was used for communication while the spectrum of 5.8 GHz was for wireless powering. In [19], a WPT system with data transmission was designed, where the power and data links have different carriers. A theoretical isolation level of 50 dB was achieved but without experimental validations. On the other hand, by combining the time-division duplex (TDD) technique with multiple-input multiple-output (MIMO) technique [20], power transfer and data delivery were carried out at different time intervals. However, facing to the growing shortage of spectral resources, it would be of great significance to facilitate the power and data transfer simultaneously within a single frequency channel. Besides, for the far-field application, a higher isolation level between the local power and data links is critical because of the weakly received signal, as compared with those for inductive-based wireless powering transfers.

To realize a highly efficient system for the far-field data transfer and power delivery, the in-band full-duplex scenario is an alternative. In an in-band full-duplex system, simultaneously bidirectional transmitting can be achieved by using a single carrier. Thus, the spectrum efficiency can be doubled theoretically compared with the TDD- and FDD-based schemes [21]–[25]. Fig. 1 shows the block diagram of a wireless sensor system with the far-field WPT and data transfer based on the in-band full-duplex scheme. The scheme employs the same frequency carrier to deliver power and data simultaneously. To realize a full-duplex system, one challenge is the suppression of the strong leakage (called the self-interference) that mainly results from the mutual coupling between the local transmitting and receiving antennas [21]–[25]. It is known that orthogonal polarizations such as vertical and horizontal polarizations can result in some isolations naturally, thus the utilization of

Manuscript received April 15, 2018; revised July 6, 2018; accepted August 10, 2018. Date of publication August 14, 2018; date of current version November 12, 2018. This work was supported in part by the National Natural Science Foundation of China (NSFC) under Grants 61271025 and 61601063. The review of this paper was coordinated by Dr. K. Adachi. *(Corresponding author: Jia-Lin Li.)*

The authors are with the School of Physics, University of Electronic Science and Technology of China, Chengdu 610054, China (e-mail: ymzhang@std.uestc.edu.cn; jialinli@uestc.edu.cn).

This paper has supplementary downloadable multimedia material available at http://ieeexplore.ieee.org provided by the authors. This material is 7.64 MB in size.

Color versions of one or more of the figures in this paper are available online at http://ieeexplore.ieee.org.

Digital Object Identifier 10.1109/TVT.2018.2865415

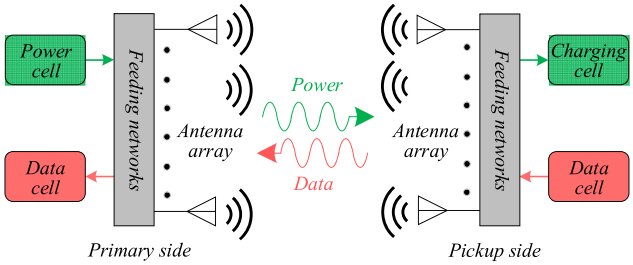

Fig. 1. Block diagram of a wireless sensor system with simultaneously far-field WPT and data transfer based on an in-band full-duplex scheme.

dual-polarized antennas with enhanced isolations would be attractive for full-duplex applications. In [21], an isolation improvement scheme for a dual-polarized rectangular patch antenna was designed based on planar wavetraps, where the achieved isolation is over 65 dB at 2.56 GHz. In [22], a full-duplex scheme using a single dual-polarized antenna was designed. The isolation of 88 dB was achieved around 2.4 GHz by employing the combination of antenna-based suppression and digital cancellation techniques. For single-antenna systems, the techniques provided in [21] and [22] can be developed readily owing to the simple coupling. Nevertheless, for the antenna array scenarios, it is still a challenge to suppress the complicated mutual coupling among antenna elements. In [26], [27], 4 × 4 and 2 × 2 dual-polarized antenna arrays using stacked configurations were studied respectively, where the realized inter-port isolations were less than 52 dB. For the far-field powering and communication applications, especially for the directive powering beaming at microwave frequencies, antenna arrays characterizing narrow beamwidths and high directivities are more attractive and efficient [28], [29].

In this paper, an in-band full-duplex scheme based on a dual-polarized antenna array is studied for simultaneously far-field power transfer and communication in wireless sensor systems, where the independence of the transmitting link and receiving link corresponds to the high inter-port isolation, thus being the primary challenge of such a scheme. We propose and discuss an RF front-end architecture composed of a dual polarized antenna array integrated with symmetrical feeding networks, characterizing a very high isolation level to ensure the power transfer and data delivery simultaneously. For demonstration purposes, an on-board prototype is developed and examined, and transmission experiments are carried out. Results from the simulations and experiments indicate the demonstrator exhibits a high isolation level of over 71 dB, low insertion losses and desired radiation responses.

II. Analyses of Self-Interference Cancellation

Here, a 1 × 2 dual-polarized antenna array with improved isolation performance is proposed as illustrated in Fig. 2. The array uses a symmetrical geometry and consists of two dual-polarized antenna elements. Each antenna element includes three stacked substrates and one air layer. Patch 1 and patch 2 are realized on the top of substrate 2 and the bottom of substrate 3, respectively. The air layer is positioned between substrates 2 and 3, and

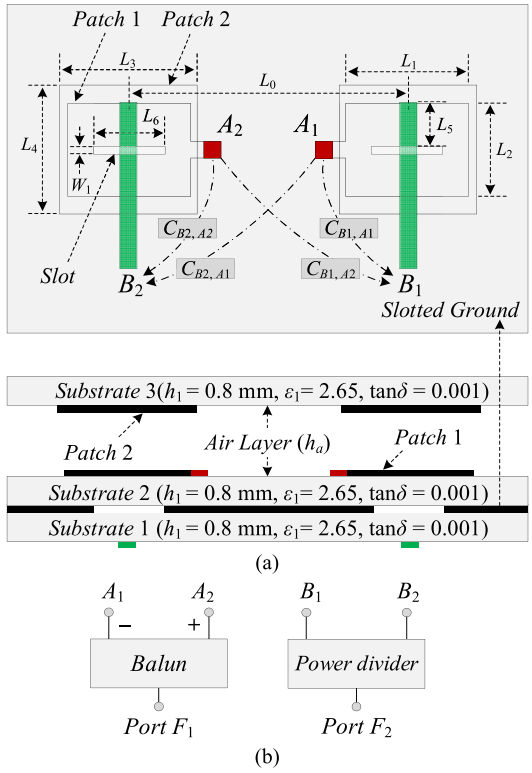

Fig. 2. (a) Configurations of the proposed 1 × 2 dual-polarized antenna array. (b) The feeding network.

a shared ground plane with rectangular slots is inserted between the substrates 1 and 2. The three substrates are all F4BME265 substrates, with a relative permittivity and a loss tangent of 2.65 and 0.001, respectively. For each element, one polarization is excited through the slot coupling where the feeding line is placed on the bottom of the substrate 1, and the other is the utilization of 50-Ω microstrip line-based side excitation that is on the same plane as patch 1. Thus, each polarization is actually excited by two elements (marked as A_1 and A_2, B_1 and B_2) in the array. Since a parasitical patch (patch 2) is employed for the antenna element, two resonances will be generated, leading to an improved impedance bandwidth compared with the typically single-layer patch antenna. By adjusting the sizes of the patches and the thickness of the air layer, impedance matching can be readily realized. For the feeding network, one power divider with equal outputs and one balun are employed to construct the feeding network, as shown in Fig. 2(b). It is seen from Fig. 2(a) that there are four coupling paths within the array, and the self- interference resulting from these couplings can be well suppressed by using the proposed architecture, as shown below.

Here we set the port F_1 and port F_2 as the transmitting port and receiving port respectively without loss of generality. Thus, the self-interference due to the leakage through the mutual coupling from port F_1 to port F_2 is studied. The coupling matrix of the array can be described as

$$C_{F2,F1} = \begin{bmatrix} C_{B1,A1} & C_{B1,A2} \\ C_{B2,A1} & C_{B2,A2} \end{bmatrix} \quad (1)$$

where $C_{Bi,Aj}$ is the coupling coefficient between elements B_i and A_j. Owing to the symmetry, we have

$$\begin{cases} C_{B1,A1} = C_{B2,A2} \\ C_{B1,A2} = C_{B2,A1} \end{cases} \tag{2}$$

Based on the proposed feeding network depicted in Fig. 2(b), the transmission matrixes at the center frequency, from ports F_1 and F_2, to the relative elements are respectively given by

$$S_{F1} = \left[|S_n| e^{-j(\varphi_1+\varphi_e)} \quad |S_p| e^{-j(\varphi_1+\pi)} \right] \tag{3}$$

$$S_{F2} = \left[S_{pd} e^{-j\varphi_2} \quad S_{pd} e^{-j\varphi_2} \right] \tag{4}$$

where φ_1 and φ_2 are the excitation phases at ports F_1 and F_2, respectively; S_n and S_p are the transmission coefficients of the balun at the negative $(-)$ and positive $(+)$ ports, respectively; φ_e is the phase imbalance between the two outputs of the balun; S_{pd} is the transmission coefficient of the power divider. Hence, the transmission coefficient $S_{F2,F1}$ from port F_1 to port F_2 can be evaluated from (1)–(4), expressed as

$$\begin{aligned} S_{F2,F1} &= S_{F2} C_{F2,F1} S_{F1}^T \\ &= \left[|S_n| e^{-j(\varphi_1+\varphi_e)} + |S_p| e^{-j(\varphi_1+\pi)} \right] \\ &\quad \times \left(C_{B1,A1} + C_{B1,A2} \right) S_{pd} \end{aligned} \tag{5}$$

Assuming that both magnitude and phase imbalances are zero for the balun, that is, $\varphi_e = 0°$ and $S_n = S_p$, the transmission coefficient $S_{F2,F1}$ would be zero according to (5). This implies a perfect isolation between the ports F_1 and F_2 However, in practice, a balun with the ideal division for 180° outputs is difficult to be achieved when the operation deviates from the center frequency, leading to a non-negligible influence on the cancellation level. As a result, the achievable level and operational bandwidth for a high isolation would mainly depend on the magnitude and phase imbalances of the balun.

For quantitative analyses, cancellation level for two paths of the coupling signals with the same magnitude and out of phase is evaluated. Taking the coupling $C_{B1,A1}$ and $C_{B2,A2}$ as the case study, the transmission coefficient S_1 from port F_1 to port F_2 through the two coupling paths can be given based on (1)–(5), which is expressed as

$$S_1 = \left[|S_n| e^{-j(\varphi_1+\varphi_e)} + |S_p| e^{-j(\varphi_1+\pi)} \right] C_{B1,A1} S_{pd} \tag{6}$$

Subsequently, with given errors of the magnitude and phase imbalances, the cancellation level for the coupling $C_{B1,A1}$ and $C_{B2,A2}$ can be evaluated. Fig. 3 depicts some calculated results under several magnitude and phase errors. It is clearly seen that both the magnitude and phase errors have important influence on the cancellations. For instance, with a maximal 0.2-dB error in magnitude and a ±1.8° error in phase, cancellation levels of over 35 dB can be observed. On the other hand, if the phase error is over ±4°, the cancellation level would be less than 28 dB theoretically. As a consequence, if the differential feeding networks shown in Fig. 2 with small magnitude and phase imbalances within a wide frequency band can be developed, good self-interference suppressions in a wide band can be achieved.

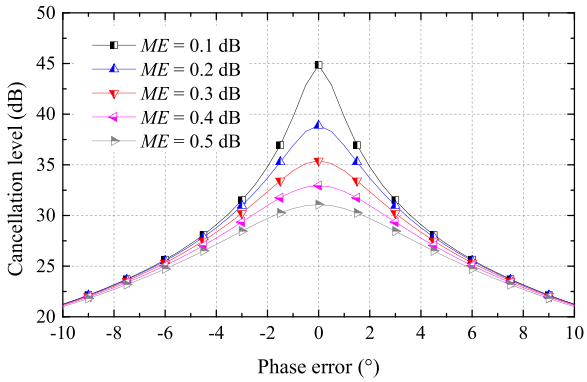

Fig. 3. Calculated cancellation level of two out-of-phase signals with certain errors in phase and magnitude, where *ME* denotes the magnitude error.

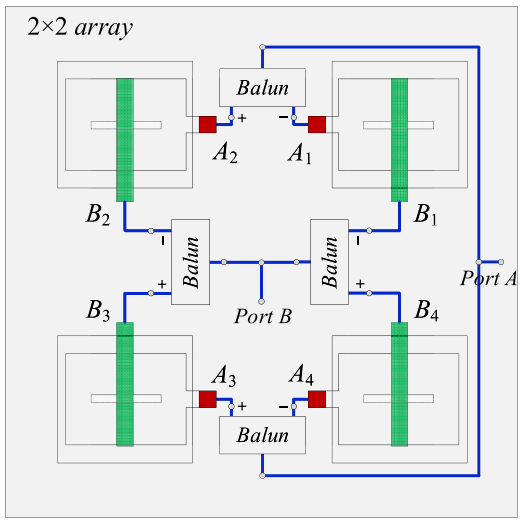

Fig. 4. Configuration of the proposed 2 × 2 dual-polarized antenna array.

Based on the proposed 1 × 2 dual-polarized array scheme, a 2 × 2 dual-polarized antenna array is presented with improved isolation performance, as shown in Fig. 4. For the proposed 2 × 2 array, the coupling matrix can be given by

$$C_{B,A} = \begin{bmatrix} C_{B1,A1} & C_{B1,A2} & C_{B1,A3} & C_{B1,A4} \\ C_{B2,A1} & C_{B2,A2} & C_{B2,A3} & C_{B2,A4} \\ C_{B3,A1} & C_{B3,A2} & C_{B3,A3} & C_{B3,A4} \\ C_{B4,A1} & C_{B4,A2} & C_{B4,A3} & C_{B4,A4} \end{bmatrix} \tag{7}$$

Due to the symmetry, we have

$$\begin{cases} C_{B1,A1} = C_{B2,A2} = C_{B3,A3} = C_{B4,A4} \\ C_{B1,A2} = C_{B2,A1} = C_{B3,A4} = C_{B4,A3} \\ C_{B1,A3} = C_{B2,A4} = C_{B3,A1} = C_{B4,A2} \\ C_{B1,A4} = C_{B2,A3} = C_{B3,A2} = C_{B4,A1} \end{cases} \tag{8}$$

Following the discussion for the derivation of (5), the transmission coefficient $S_{B,A}$ from port A to port B can be evaluated

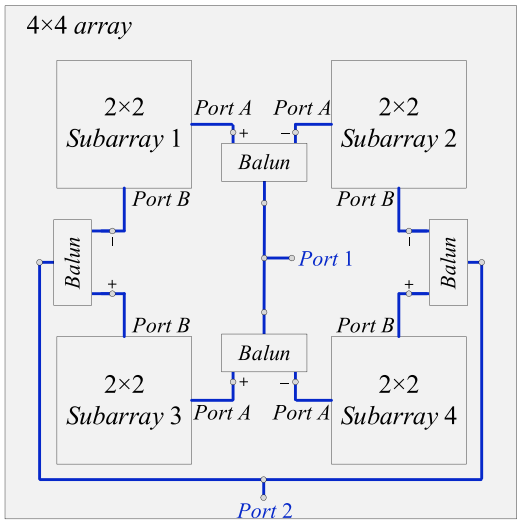

Fig. 5. Configuration of the proposed 4 × 4 dual-polarized antenna array, where the 2 × 2 array shown in Fig. 4 is employed as the 2 × 2 subarray.

based on (7) and (8), expressed as

$$S_{B,A} = \left[|S_n|\, e^{-j(\varphi_A+\varphi_e)} + |S_p|\, e^{-j(\varphi_B+\pi)}\right]^2 C_M \tag{9a}$$

$$C_M = C_{B1,A1} + C_{B1,A2} + C_{B1,A3} + C_{B1,A4} \tag{9b}$$

Interestingly, there is a square item in (9a) as compared to (5). This implies that the leakage from port A to port B through each coupling path within the 2 × 2 antenna array would be canceled twice, leading to an improved inter-port isolation. Finally, a 4 × 4 dual-polarized antenna with symmetrical configuration is proposed as shown in Fig. 5, where the 2 × 2 array illustrated in Fig. 4 is employed as the 2 × 2 subarray. Based on the above discussions, the transmission coefficient $S_{2,1}$ between ports 1 and 2 in the 4 × 4 array can be readily derived, as given by

$$S_{2,1} = \left[|S_n|\, e^{-j(\varphi_A+\varphi_e)} + |S_p|\, e^{-j(\varphi_B+\pi)}\right]^4 C_{MF} \tag{10}$$

where C_{MF} is a coupling-coefficient-related item. It is seen that there is a quadruplicate item in the expression of the coefficient $S_{2,1}$. This reveals that each coupling would be canceled four times. Assuming that an improved level of 30 dB is realized for each cancellation according to the study in Fig. 3, the theoretically improvements on the isolation for the proposed 1 × 2, 2 × 2, and 4 × 4 dual-polarized arrays are 30, 60, and 120 dB respectively. With a common inter-port isolation of 30 dB for a dual-polarized element, the theoretical isolations would be 60, 90, and 150 dB. Actually, it is impossible to realize such a high isolation level (>90 dB), since the complicated mutual coupling within the feeding network, the surface current, the fabrication tolerance and the non-ideal environment would degrade the isolation.

The above discussions indicate that the self-interference resulting from the complicated mutual couplings can be suppressed theoretically by using the proposed scheme. To demonstrate the scheme, an on-board prototype at 5.2 GHz is developed and examined. Furthermore, based on the developed prototypes, experiments for simultaneous power and data transmission are carried out and analyzed.

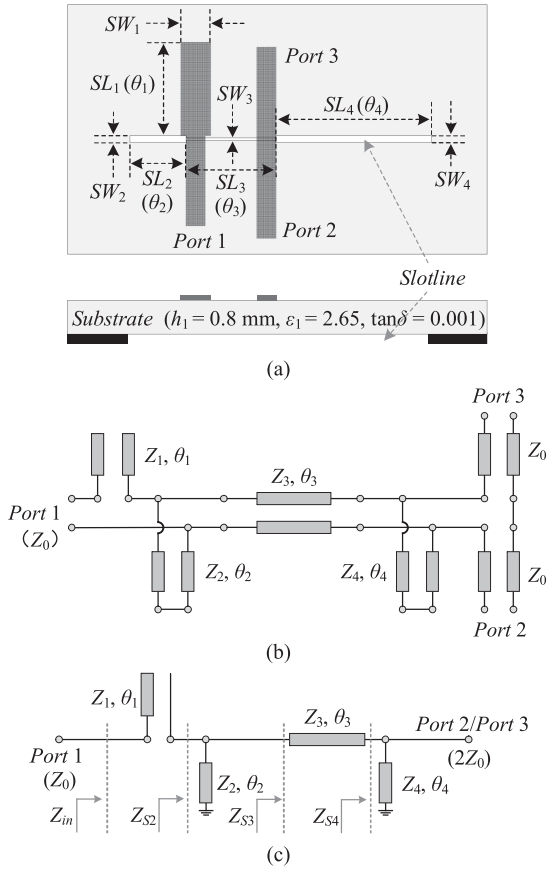

Fig. 6. (a) Configuration of the proposed wide-band balun. (a) Simplified equivalent circuit, where $\theta_1 = 45°, \theta_2 = 30°, \theta_3 = 60°, \theta_4 = 90°$ (at the center frequency of f_0). (c) Simplified 2-port model derived from Fig. 4(b).

III. Design Descriptions of the Demonstrator

A. Wideband Balun

As discussed above, a well-designed feeding network with small magnitude and phase imbalances are important to widen the bandwidth. To achieve a small phase imbalance within a wide band, one of the methods is the utilization of phase compensation technique at the cost of bulky system and large magnitude imbalances [30]. In this work, a compact slotline-based balun, featuring wide impedance bandwidth as well as small magnitude and phase imbalances, is proposed for the presented scheme. Fig. 6(a) illustrates the configuration of the proposed balun that includes one half-wavelength slotline and two transmission lines positioned cross the slotline. The simplified three-port equivalent circuit of the balun is shown in Fig. 6(b), where the electrical lengths θ_i $(i = 1, 2, 3, 4)$ refer to the center frequency f_0. It can be observed that the phase difference between the two output interfaces would be 180° over a wide frequency band because of the operational characteristics of the slotline. On the other hand, in order to show the impedance matching performance, a two-port model derived from Fig. 6(b) is constructed, as depicted in Fig. 6(c). The input impedance Z_{in}

seen looking into the output interface versus frequency f can be expressed as

$$Z_{in} = \frac{Z_1}{j\tan(\theta_1 f/f_0)} + Z_{S2} \tag{11a}$$

$$Z_{S2} = \frac{jZ_2\tan(\theta_2 f/f_0)\cdot Z_{S3}}{jZ_2\tan(\theta_2 f/f_0) + Z_{S3}} \tag{11b}$$

$$Z_{S3} = Z_3\frac{Z_{S4} + jZ_3\tan(\theta_3 f/f_0)}{Z_3 + jZ_{S4}\tan(\theta_3 f/f_0)} \tag{11c}$$

$$Z_{S4} = \frac{jZ_4\tan(\theta_4 f/f_0)\cdot 2Z_0}{jZ_4\tan(\theta_4 f/f_0) + 2Z_0} \tag{11d}$$

where Z_{S2}, Z_{S3}, Z_{S4} are the input impedances as marked in Fig. 6(c). The zero reflection corresponds to

$$Z_{in} = Z_0. \tag{12}$$

From Eqs. (11) and (12), it is found that two resonant modes distributed symmetrically on the two sides of the center frequency can be excited, resulting in a wide impedance bandwidth response. The resonant modes can be tuned on the basis of the tunable parameters Z_1, Z_2, Z_3, and Z_4. Fig. 7(a) and (b) depict the calculated frequency responses based on the equivalent circuit shown in Fig. 6(b) under some specified resonant frequencies. It is clearly seen that there are two resonances around the center frequency. Meanwhile, a larger spacing between the two resonances corresponds to a wider transmission bandwidth but suffering from slightly poorer in-band return losses. The phase imbalances, as illustrated in Fig. 7(b), exhibit wide bandwidth responses. On the other hand, the magnitudes of the two outputs are of small imbalance.

With these analyses, it can be observed that the proposed balun features small magnitude and phase imbalances within a wide frequency band. Consequently, a slotline-based balun centered at 5.2 GHz is developed referring to Fig. 6. The substrate parameters are given in Fig. 6(a). The optimal sizes are (unit: mm): $SL_1 = 5.5$, $SL_2 = 3.7$, $SL_3 = 7.5$, $SL_4 = 10.2$, $SW_1 = 3.3$, $SW_2 = 1.1$, $SW_3 = 0.3$, $SW_4 = 1.1$. Figs. 7(c) and 7(d) provide the full-wave simulated frequency responses. It is seen that the fractional bandwidth is over 70% from 3.3 to over 7.0 GHz referring to $|S_{1,1}| \leq -10$ dB, and over 40% from 3.8 to 5.9 GHz referring to $|S_{1,1}| \leq -20$ dB. The magnitude and phase imbalances are within ± 0.2 dB and $\pm 1.5°$ among the studied frequency band, respectively. With this performance, it can be incorporated into the proposed in-band full-duplex scheme shown in Figs. 4 and 5.

B. 2 × 2 and 4 × 4 Dual-Polarized Antenna Arrays

In this part, the proposed 2 × 2 and 4 × 4 dual-polarized arrays shown in Figs. 4 and 5 are both modeled and discussed to show the realized isolation performance. The geometric dimensions of the proposed 2 × 2 demonstrator are (unit: mm): $L_0 = 40.4$, $L_1 = 17.6$, $L_2 = 13.2$, $L_3 = 19.7$, $L_4 = 19.4$, $L_5 = 6.0$, $L_6 = 12.7$, $W_1 = 0.9$. The center distance between adjacent elements is $0.7\lambda_0$, where λ_0 is the free space wavelength at the center

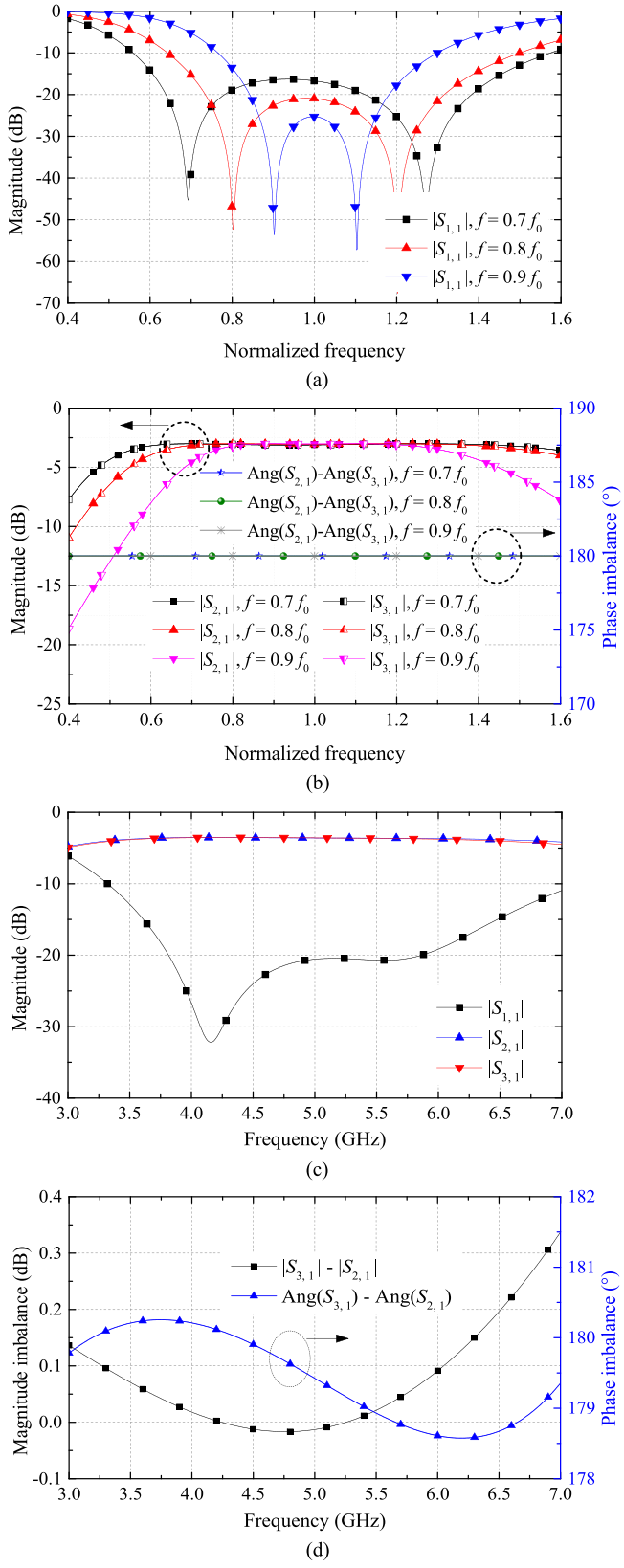

Fig. 7. (a) Impedance matching performance. (b) Transmission responses of the three-port model under some specified zero reflections. (c) Simulated S-parameters of the designed balun centered at 5.2 GHz. (d) Simulated magnitude and phase imbalances of the designed balun.

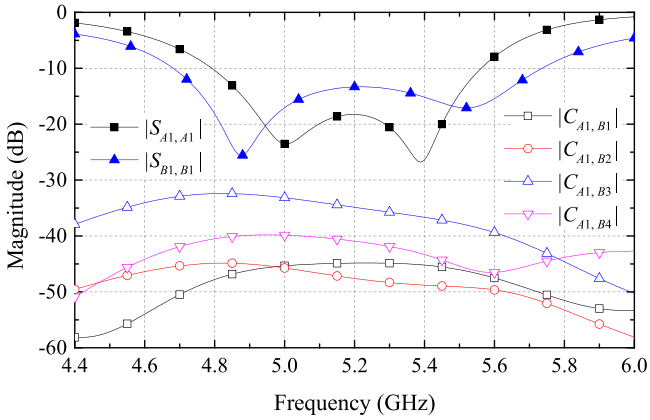

Fig. 8. Simulated S-parameters of the proposed array described in Fig. 4 without using the feeding network.

frequency of 5.2 GHz. The parameters of the substrates are given in Fig. 2, and the air layer is 4 mm. Presented in Fig. 8 is the full-wave simulated frequency responses of the array shown in Fig. 4 without using the feeding network. It is observed that the maximum coupling is approximately −32.5 dB around 4.8 GHz. On the other hand, it would be seen that by using the proposed balun, a theoretical cancellation level of over 35 dB could be achieved within a range from 4.4 to 6.0 GHz for each coupling, as described in Fig. 3.

Further, Fig. 9(a) shows the layout of the proposed 2 × 2 dual-polarized antenna array including the balun-based differential feeding network. The simulated impedance matching performance and the isolation between the two ports of the array are depicted in Fig. 9(c). The achieved isolation is over 55 dB from 4.7 to over 6.0 GHz. Although distinct difference between $S_{A,A}$ and $S_{B,B}$ is observed which mainly due to the different feeding techniques, the shared impedance bandwidth still exhibits a wide-band response from 4.9 to 5.65 GHz. It is seen that the simulated isolation does not achieve the theoretically high level of over 90 dB, mainly due to the unavoidable tolerances/errors as discussed in Section II. Besides, as shown in Fig. 9(a), it is reasonable to conclude that the coupling coefficients from slot S_1 and slot S_2 to port A (marked as C_{S1} and C_{S2} respectively) are not the same because of the asymmetrical layout of the feeding networks, leading to a deterioration in isolation performance. As studied in Section II, by using the 2 × 2 array to construct the 4 × 4 array, the inter-port isolation can be further improved. On the other hand, for the 2 × 2 array, the 3-dB beam widths of the radiation patterns for the two ports are both 36° as recorded in Fig. 9(d). It is known that in general, a narrower beam results in a higher gain, which is more attractive for far-field directional transmissions. Consequently, to further improve the inter-port isolation and narrow down the 3-dB beam widths of the radiation patterns for far-field directional transmissions, the 4 × 4 dual-polarized antenna array shown in Fig. 5 is developed, as illustrated in Fig. 10. In view of the quasi-symmetrical feeding network, the mentioned couplings (C_{S1} and C_{S2}) would be canceled. Following the discussions in Section II, similar analyses can be carried out and for brevity, they are not detailed here. Further, parallel lines are utilized to suppress the couplings within

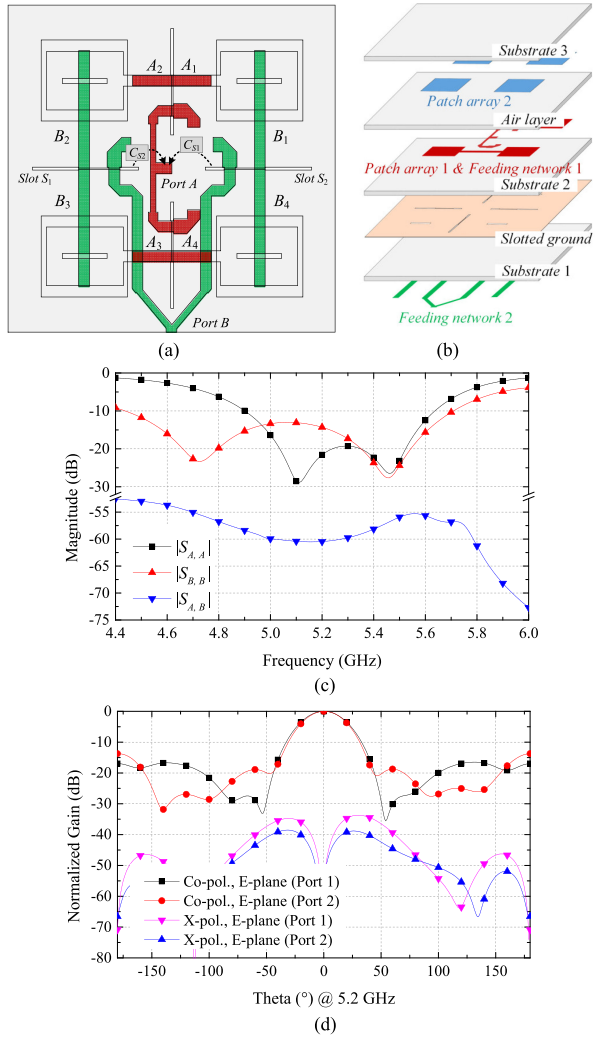

Fig. 9. (a) Configuration. (b) 3D view of the proposed 2 × 2 array. (c) Full-wave simulated S-parameters. (d) Radiation patterns of the array.

the feeding network. As shown in Fig. 10(c), each pair of the parallel lines is positioned to surround a slotline. Due to the symmetry, the coupling coefficients from the two sides of the slotline to the two parallel lines are equal. On the other hand, it is known that the electric fields distributed at the two sides of the slotline are out of phase. Subsequently, it can be readily concluded that the two leakage paths from the slotline to the two parallel lines would be canceled with each other at the common node of the two parallel lines, and vice versa due to the reciprocity. Thus, coupling suppression between the transmission lines and slotlines corresponding to the two ports is realized with the utilization of the parallel lines. Moreover, the feedings of the two orthogonal polarizations are simply positioned on different layers that are separated by the common ground plane, leading to reduced couplings between the transmission lines.

IV. Fabrication and Measurements

The demonstrator presented in Fig. 10 is fabricated and assembled as shown in Fig. 11, where plastic screws are utilized

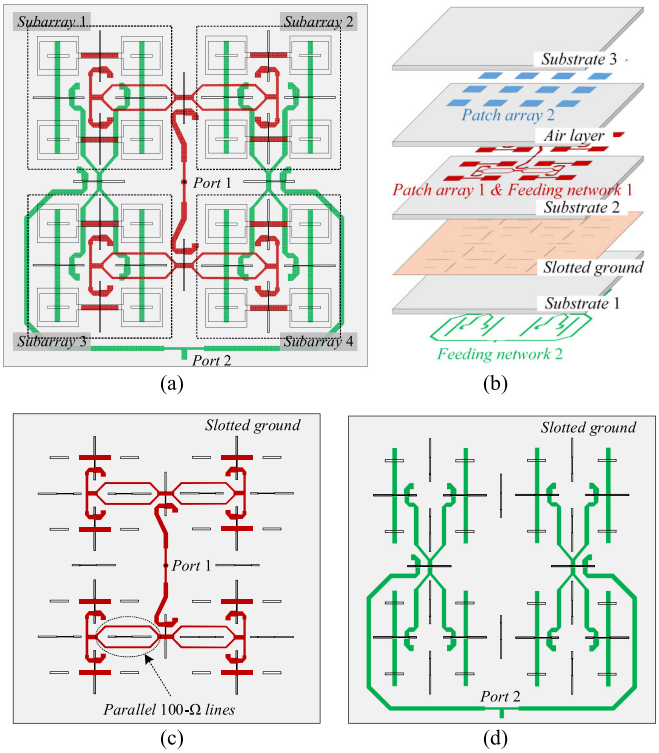

Fig. 10. (a) Configuration. (b) 3D view of the proposed 4 × 4 array. (c) Layouts of the feeding networks for port 1. (d) Layouts of the feeding networks for port 2.

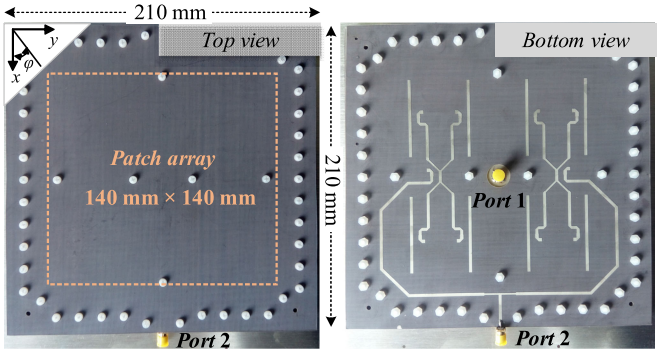

Fig. 11. Photographs of the developed demonstrator.

for fixation purposes. The overall size is 210 mm × 210 mm, and the radiation patch array has a size of 140 mm × 140 mm.

Fig. 12 plots the measured and simulated impedance matching and isolation performance of the developed demonstrator. The measured impedance bandwidth for port 1 is from 4.4 to over 6.0 GHz referring to $|S_{1,1}| \leq -10$ dB, and it is from 4.5 to 5.8 GHz for port 2. Meanwhile, it is seen that very high isolation levels are observed. Specifically, the isolation is over 65 dB within the studied frequency band, and better than 71 dB from 5.32 to 5.86 GHz, indicating a well-designed self-interference suppression. Notice that the S-parameters are measured in lab environment, the measured isolation has some degradations compared with the simulated results, which is mainly due to the practical errors and environmental reflections.

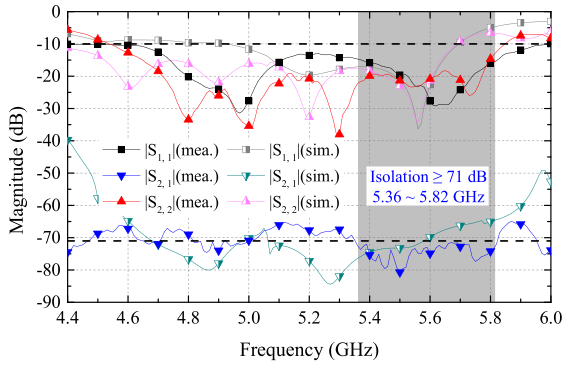

Fig. 12. Measured and simulated S-parameters of the demonstrator.

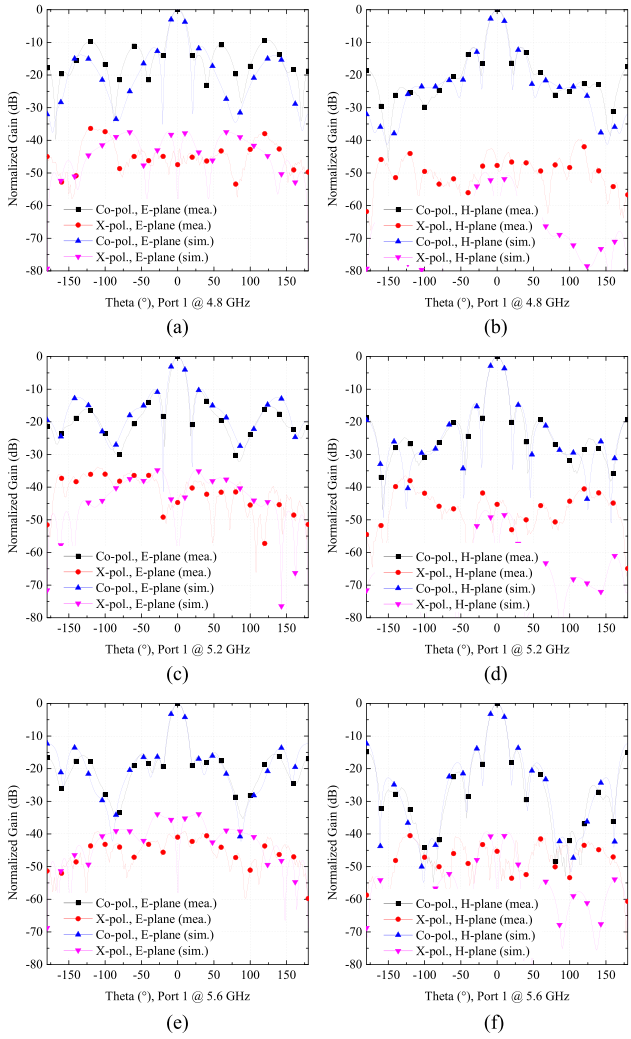

Fig. 13. Measured and simulated far-field radiation patterns of the demonstrator when port 1 is excited. (a) 4.8 GHz on E-plane. (b) 4.8 GHz on H-plane. (c) 5.2 GHz on E-plane. (d) 5.2 GHz on H-plane. (e) 5.6 GHz on E-plane. (f) 5.6 GHz on H-plane.

The far-field radiation patterns at 4.8 GHz, 5.2 GHz, and 5.6 GHz at *E*- and *H*-planes are measured. As depicted in Fig. 13, the array under port 1 excitation characterizes linearly polarized radiations with the 3-dB beam width of approximately 18° at both *E*- and *H*-planes, and the cross polarization is better than

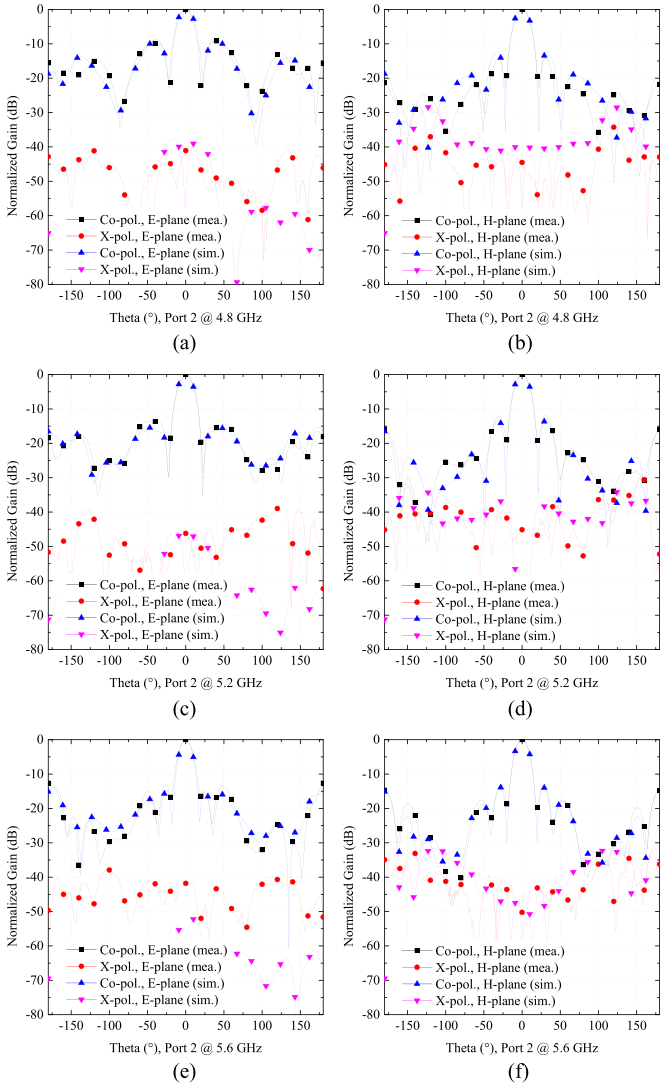

Fig. 14. Measured and simulated far-field radiation patterns of the demonstrator when port 2 is excited. (a) 4.8 GHz on E-plane. (b) 4.8 GHz on H-plane. (c) 5.2 GHz on E-plane. (d) 5.2 GHz on H-plane. (e) 5.6 GHz on E-plane. (f) 5.6 GHz on H-plane.

40 dB at the boresight for each case. It is found that the side lobes are lower than −10 dB, especially for the case for 5.6 GHz where the side lobes are less than −14 dB as shown in Fig. 13(e) and (f). Fig. 14 records the far-field radiation responses when port 2 is excited. As compared with those shown in Fig. 13, similar performance can be observed and for brevity, they are not detailed here. Also, the realized gain is investigated as described in Fig. 15. The measured data indicates that for either port 1 or port 2 excited, the gain is fluctuated between 17.0 to 19.0 dBi from 4.8 to 5.7 GHz. The simulated radiation efficiency of the proposed antenna array versus frequency is also provided in Fig. 15. Despite no measured results due to the lack of 3D-test environment, good agreement between simulations and measurements for the radiation patterns and the achieved gains could make us reasonably perceive the consistency of the efficiency. From these results, it can be observed that the measured data matches the simulated result well within the studied frequency band.

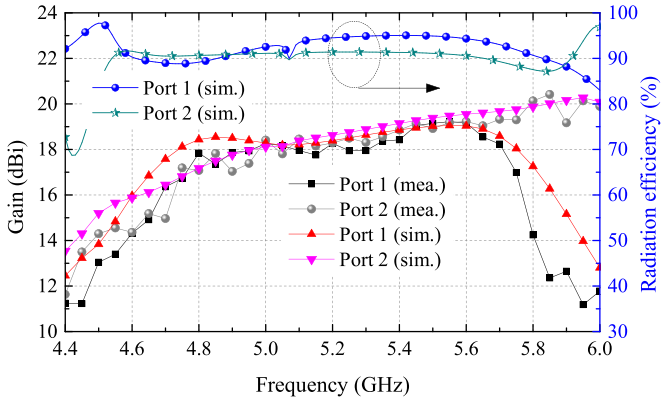

Fig. 15. Realized gain and simulated radiation efficiency of the demonstrator.

TABLE I
PERFORMANCE COMPARISONS AMONG SOME PUBLISHED AND THE PROPOSED DUAL-POLARIZED ANTENNAS

Ref./Year	[25]/2017	[26]/2015	[27]/2018	**This work**
Antenna configuration	Single element	4×4 array	2×2 array	4×4 array
Distance between adjacent elements	–	$0.8\lambda_0$	$0.75\lambda_0$	$0.7\lambda_0$
Impedance bandwidth (GHz)	2.385~2.435	22.0~26.5	11.9~15.4	4.5~5.8
Isolation bandwidth (GHz)	2.385~2.435 (> 70 dB) 2.40~2.42 (> 79 dB)	22.0~26.5 (> 35 dB)	11.9~15.4 (> 32 dB) 12.8~14.1 (> 50 dB)	4.5~5.8 (> 65 dB) 5.36~5.82 (> 71 dB)
Realized gain (dBi)	4.1	16.0	–	18.5
Radiation efficiency	50%	–	–	> 90% [a]

[a] denotes the simulated result.

For performance comparisons, some recently published dual-polarized antennas are summarized, as listed in Table I. From these reports, it is found that for a single-antenna system, a high isolation can be achieved owing to the simple coupling. However, for antenna array-based scenarios, it is difficult to enhance the isolation to over 50 dB. On the other hand, for the proposed antenna array, it has been demonstrated that the complicated mutual coupling within the array and the feeding network can be well canceled, resulting in a very high interport isolation of over 71 dB. Since only distributed components featuring low losses are employed in the presented array, the simulated radiation efficiency is over 90% for each port.

V. EXPERIMENTAL VERIFICATION FOR WIRELESS POWER TRANSFER AND DATA DELIVERY

Experiments on simultaneously power transfer and data delivery are carried out to further verify the performance of the developed demonstrator. The block diagram of the experiment setup is shown in Fig. 16(a), where two copies (marked as array A and array B) of the developed demonstrator are placed

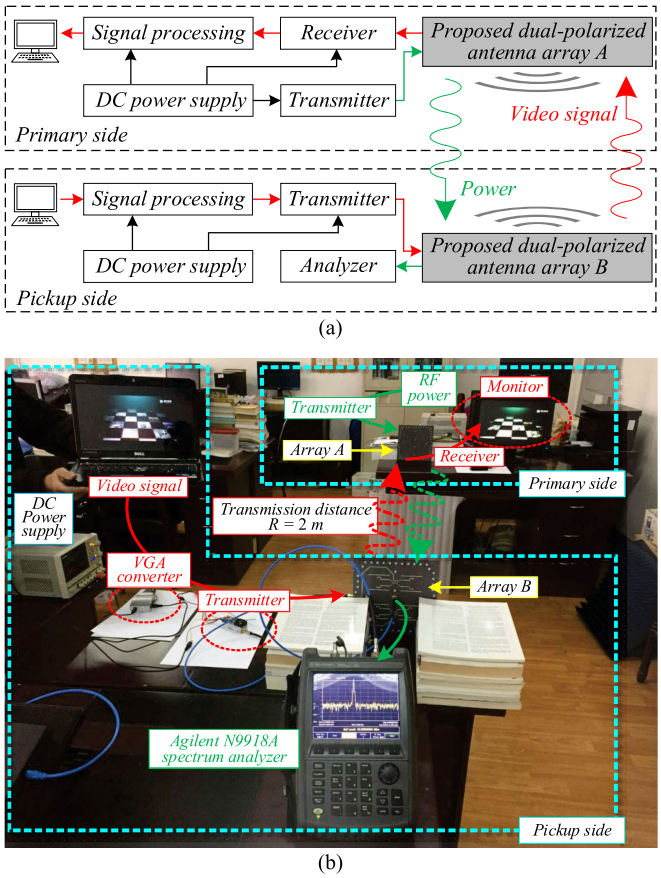

Fig. 16. (a) Block diagram of the experimental setup for simultaneously far-field wireless power and data transfer using the proposed antenna array. (b) Photo of the experimental setup.

face-to-face with matched polarizations. For the primary side (array A), microwave power generated by a microwave source directionally radiates to the free space at the boresight, and simultaneously the video signal sent from the pickup side is wirelessly received, demodulated, and displayed on a monitor through a VGA converter. As for the pickup side (array B), wireless power is received and measured by a spectrum analyzer, meanwhile, the video signal output from a computer via the VGA interface is modulated on the same frequency band as the one utilized by the power link. Notice that in the experiment, both the power transfer and data delivery share the same radio frequency (RF) carrier.

The experiment platform is pictured in Fig. 16(b), where the transmission distance is 2 m. Since the far-field region of the developed antenna array is $R > 1.475$ m, the transmission experiment is carried out under a far-field condition in this work. The channels of horizontal and vertical polarizations are driven as power and data links, respectively. In view of the extremely high isolation of over 71 dB from 5.36 to 5.82 GHz as mentioned above, the video signal is modulated around 5.645 GHz, and the same one for the WPT frequency. The output power from the receiving port of the pickup side is measured by the Agilent N9918A spectrum analyzer, as illustrated in Fig. 17 together with the one of the input at the transmitter of the primary side. It is seen that the wireless power radiated from the primary side is

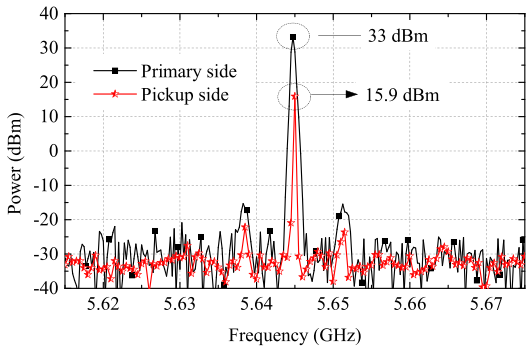

Fig. 17. Measured power received by the array B at the output interface of the pickup side together with the one input for the array A of the primary side.

33 dBm, and the received power for the pickup side is 15.9 dBm. Theoretically, the received power P_r at the pickup side can be evaluated based on the Friis radio link formula, given by

$$P_r = \frac{G_t G_r \lambda_0^2}{(4\pi R)^2} P_t, \text{(unit:W)} \tag{13}$$

where P_t is the transmitting power at the primary side, G_t and G_r are the gains of transmitting and receiving antennas, respectively, λ_0 is the wavelength in free space at the center frequency, and R is the transmission distance. In this case, the corresponding parameters are $P_t = 33$ dBm, $R = 2.0$ m, $\lambda_0 = 53.14$ mm, $G_t = G_r = 18.5$ dBi. Therefore, the received power P_r is 16.5 dBm in theory. The received RF power from measurements is 0.6 dB lower than that from the calculation. The difference can be simply attributed to the multipath fading because of the in-door environment, as illustrated in Fig. 16(b). Besides, without degrading the performance of the data link, the maximum transmitting power at the primary side can also be estimated for the given setup. Here we present the radio transmitter at the pickup side for data delivery being 20 dBm. The received power of the data link at the primary side can be calculated from (13), which is 3.5 dBm. Assuming that the receiver for the data link with a typical noise threshold of 9 dB is utilized at the primary side, the received noise power leakage from the local transmitter should be less than -5.5 dBm. Consequently, referring to the measured isolation level of 71 dB between the local transmitter and receiver as provided in Fig. 12, the input power at the primary side for power transfer should be less than 65.5 dBm.

Although the slight difference between the measurements and predications, the received power P_r is stable during the experiment, meanwhile the demodulated VGA video is smooth and fluent at the primary side. This can be seen from the short video, as the supplementary uploaded. From the experimental results and analyses, two independent channels driven under the same RF carrier for simultaneous power transfer and data delivery have been established successfully based on the developed demonstrators.

VI. Conclusion

This paper presents an in-band full-duplex scheme for far-field wireless power transfer and data delivery simultane-

ously. The proposed scheme shares the same antenna array with orthogonal polarizations for transmitting and receiving functions, where the utilized components are all passive with low losses and low costs. To demonstrate the performance of the proposed scheme, especially the cancellation of the self-interference between the transmitting and receiving paths, a prototype demonstrator at C-band has been developed and examined, theoretically and experimentally. Results indicate the developed demonstrator exhibits good performance in terms of the impedance matching, far-field radiation, and high inter-port isolation. It is believed that the proposed in-band full-duplex architecture is attractive and applicable to the wireless sensor systems to provide independent links for simultaneous power transfer and data delivery under the same RF carrier.

REFERENCES

[1] W. Xiong, X. Hu, and T. Jiang, "Measurement and characterization of link quality for IEEE 802.15.4-compliant wireless sensor networks in vehicular communications," *IEEE Trans. Ind. Inf.*, vol. 12, no. 5, pp. 1702–1713, Oct. 2016.

[2] A. Gawanmeh, "Optimizing lifetime of homogeneous wireless sensor networks for vehicular monitoring," in *Proc. Int. Conf. Connected Veh. Expo*, Vienna, Austria, Nov. 2014, pp. 980–985.

[3] B. A. B. Granda, L. A. B. Belduma, E. J. C. González, and A. F. S. Sarango, "Designing a wireless sensor network for vehicular traffic and CO_2 pollution monitoring in an urban area," in *Proc. Latin-Amer. Conf. Commun.*, Guatemala City, Guatemala, Nov. 2017, pp. 1–6.

[4] S.-C. Hu, Y.-C. Wang, C.-Y. Huang, and Y.-C. Tseng, "A vehicular wireless sensor network for CO_2 monitoring," in *Proc. IEEE Sens.*, Christchurch, New Zealand, Oct. 2009, pp. 1498–1501.

[5] J. Ho, S. Kim, and A. Poon, "Midfield wireless powering for implantable systems," *Proc. IEEE*, vol. 101, no. 6, pp. 1369–1378, May 2013.

[6] X. Zhu, W. Zeng, and C. Xiao, "Precoder design for simultaneous wireless information and power transfer systems with finite-alphabet inputs," *IEEE Trans. Veh. Technol.*, vol. 66, no. 10, pp. 9085–9097, Oct. 2017.

[7] N. Zhao, Y. Cao, F. R. Yu, Y. Chen, M. Jin, and V. C. M. Leung, "Artificial noise assisted secure interference networks with wireless power transfer," *IEEE Trans. Veh. Technol.*, vol. 67, no. 2, pp. 1087–1098, Feb. 2018.

[8] J. Park, B. Clerckx, C. Song, and Y. Wu, "An analysis of the optimum node density for simultaneous wireless information and power transfer in AD Hoc networks," *IEEE Trans. Veh. Technol.*, vol. 67, no. 3, pp. 2713–2726, Mar. 2018.

[9] X. Di, K. Xiong, P. Fan, and H.-C. Yang, "Simultaneous wireless information and power transfer in cooperative relay networks with rateless codes," *IEEE Trans. Veh. Technol.*, vol. 66, no. 4, pp. 2981–2996, Apr. 2017.

[10] D. Ahn, S. Kim, J. Moon, and I.-K. Cho, "Wireless power transfer with automatic feedback control of load resistance transformation," *IEEE Trans. Power Electron.*, vol. 31, no. 11, pp. 7876–7886, Nov. 2016.

[11] W. Jin, A. T. L. Lee, S. Li, S.-C. Tan, and S. Y. Hui, "Low-power multichannel wireless transmitter," *IEEE Trans. Power Electron.*, vol. 33, no. 6, pp. 5016–5028, Jun. 2018.

[12] C.-C. Huang and C.-L. Lin, "Wireless power and bidirectional data transfer scheme for battery charger," *IEEE Trans. Power Electron.*, vol. 33, no. 6, pp. 4679–4689, Jun. 2018.

[13] E. Falkenstein, D. Costinett, R. Zane, and Z. Popovic, "Far-field RF-powered variable duty cycle wireless sensor platform," *IEEE Trans. Circuits Syst. II, Express Briefs*, vol. 58, no. 12, pp. 822–826, Dec. 2011.

[14] Z. Popovi, E. A. Falkenstein, D. Costinett, and R. Zane, "Low-power far-field wireless powering for wireless sensors," *Proc. IEEE*, vol. 101, no. 6, pp. 1397–1409, May 2013.

[15] Z. Yan, Z. Xiang, L. Wu, and B. Wang, "Study of wireless power and information transmission technology based on the triangular current waveform," *IEEE Trans. Power Electron.*, vol. 33, no. 2, pp. 1368–1377, Feb. 2018.

[16] I. Orikumhi, C. Y. Leow, and Z. Ding, "Wireless information and power transfer in MIMO virtual full-duplex relaying system," *IEEE Trans. Veh. Technol.*, vol. 66, no. 12, pp. 11001–11010, Dec. 2017.

[17] K. Li, W. Ni, L. Duan, M. Abolhasan, and J. Niu, "Wireless power transfer and data collection in wireless sensor networks," *IEEE Trans. Veh. Technol.*, vol. 67, no. 3, pp. 2686–2697, Mar. 2018.

[18] J. Wu, C. Zhao, Z. Lin, J. Du, Y. Hu, and X. He, "Wireless power and data transfer via a common inductive link using frequency division multiplexing," *IEEE Trans. Ind. Electron.*, vol. 62, no. 12, pp. 7810–7820, Jul. 2015.

[19] Y. G. Su, W. Zhou, A. P. Hu, C. S. Tang, S. Y. Xie, and Y. Sun, "Full-duplex communication on the shared channel of a capacitively coupled power transfer system," *IEEE Trans. Power Electron.*, vol. 32, no. 4, pp. 3229–3239, Apr. 2017.

[20] X. Chen, X. Wang, and X. Chen, "Energy-efficient optimization for wireless information and power transfer in large-scale MIMO systems employing energy beamforming," *IEEE Wireless Commun. Lett.*, vol. 2, no. 6, pp. 667–670, Dec. 2013.

[21] M. Heino, S. N. Venkatasubramanian, C. Icheln, and K. Haneda, "Design of wavetraps for isolation improvement in compact in-band full-duplex relay antennas," *IEEE Trans. Antennas Propag.*, vol. 64, no. 3, pp. 1061–1070, Mar. 2016.

[22] M. S. Amjad, H. Nawaz, K. Özsoy, Ö. Gürbüz, and I. Tekin, "A low-complexity full-duplex radio implementation with a single antenna," *IEEE Trans. Veh. Technol.*, vol. 67, no. 3, pp. 2206–2218, Mar. 2018.

[23] C.-X. Mao, S. Gao, and Y. Wang, "Dual-band full-duplex Tx/Rx antennas for vehicular communications," *IEEE Trans. Veh. Technol.*, vol. 67, no. 5, pp. 4059–4070, May 2018, doi: 10.1109/TVT.2017.2789250.

[24] R. Li, A. Masmoudi, and T. L. Ngoc, "Self-interference cancellation with nonlinearity and phase-noise suppression in full-duplex systems," *IEEE Trans. Veh. Technol.*, vol. 67, no. 3, pp. 2118–2129, Mar. 2018.

[25] H. Nawaz and I. Tekin, "Dual-Polarized, differential fed microstrip patch antennas with very high interport isolation for full-duplex communication," *IEEE Trans. Antennas Propag.*, vol. 65, no. 12, pp. 7355–7360, Dec. 2017.

[26] M. A. Islam and N. C. Karmakar, "A 4×4 dual polarized mm-wave ACMPA array for a universal mm-wave chipless RFID tag reader," *IEEE Trans. Antennas Propag.*, vol. 63, no. 4, pp. 1633–1640, Apr. 2015.

[27] W. Wang, J. Wang, A. Liu, and Y. Tian, "A novel broadband and high-isolation dual-polarized microstrip antenna array based on quasi-substrate integrated waveguide technology," *IEEE Trans. Antennas Propag.*, vol. 66, no. 2, pp. 951–956, Feb. 2018.

[28] N. Shinohara and H. Matsumoto, "Experimental study of large rectenna array for microwave energy transmission," *IEEE Trans. Microw. Theory Techn.*, vol. 46, no. 3, pp. 261–268, Mar. 1998.

[29] W. C. Brown, "The history of power transmission by radio waves," *IEEE Trans. Microw. Theory Techn.*, vol. MTT-32, no. 9, pp. 1230–1242, Sep. 1984.

[30] S.-Y. Yin, J.-L. Li, C.-G. Sun, and H. Li, "Dual-band rat-race hybrid with phase compensation," *Electromagnetics*, vol. 38, no. 3, pp. 200–206, Mar. 2018.

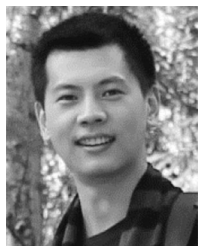

Yi-Ming Zhang (S'17) received the M.S. degree from the School of Physical Electronics, University of Electronic Science and Technology of China, Chengdu, China, in 2014. He is currently working toward the Ph.D. degree from the same university.

His current research interests are focused on MIMO antenna decoupling and single-channel full-duplex communications including antenna-based and analog-based self-interference suppressions.

Jia-Lin Li received the M.S. degree from the University of Electronic Science and Technology of China (UESTC), Chengdu, China, in 2004, and the Ph.D. degree from the City University of Hong Kong, Hong Kong, in 2009, both in electronic engineering.

From September 2005 to August 2006, he was a Research Associate with the Wireless Communication Research Center, City University of Hong Kong. Since September 2009, he has been with the School of Physical Electronics, UESTC, where he is currently a Professor. His research interests include microwave/millimeter-wave antenna and arrays, circuits and systems, interactions between microwave and complex medium, and so on.